Temperature control of ion guiding through insulating capillaries

E. Gruber, G. Kowarik, F. Ladinig, J. P. Waclawek, D. Schrempf, and F. Aumayr*
Institute of Applied Physics, TU Wien–Vienna University of Technology, 1040 Vienna, Austria, European Union

R. J. Bereczky and K. Tőkési
Institute of Nuclear Research of the Hungarian Academy of Sciences (ATOMKI), 4001 Debrecen, Hungary, European Union

P. Gunacker, T. Schweigler, C. Lemell, and J. Burgdörfer
Institute of Theoretical Physics, TU Wien–Vienna University of Technology, 1040 Vienna, Austria, European Union
(Received 25 September 2012; published 4 December 2012)

Guiding of highly charged ions through tilted capillaries promises to develop into a tool to efficiently collimate and focus low-energy ion beams to sub-micrometer spot size. One control parameter to optimize guiding is the residual electrical conductivity of the insulating material. Its strong, nearly exponential temperature dependence is the key to transmission control and can be used to suppress transmission instabilities arising from flux fluctuations of incident ions which otherwise would lead to Coulomb blocking of the capillary. We demonstrate the strong dependence of transmission of Ar^{7+} ions through a single macroscopic glass capillary on temperature and ion flux. Results in the regime of dynamical equilibrium can be described by balance equations in the linear-response regime.

DOI: 10.1103/PhysRevA.86.062901 PACS number(s): 34.35.+a, 79.20.Rf

I. INTRODUCTION

Placing or implanting a single ion at a desired point on a substrate surface with nanometer-scale precision would be highly desirable for many novel applications such as, e.g., nanomodifications of surfaces [1–4], fabrication of solid state qubit arrays [5,6], or nanosurgery of living cells [7]. Slow highly charged ions (HCIs) are of particular interest due to their high potential energy which is primarily deposited in a nanometer-sized volume centered at the impact site resulting in the emission of a large number of secondary particles [8,9]. Impacting on insulating materials, slow HCIs may induce the formation of stable hillock- or crater-type nanostructures [3,4,10,11]. While the emission of a large number of electrons allows for detection of each ion impact with unit efficiency and therefore single ion hit monitoring [12], the morphology and size of the resulting material modification can be tuned by the charge state of the incoming highly charged ion [13]. The main challenge remaining is to control the ion impact point as precisely as possible. One possibility for the preparation of a well-focused HCI nanobeam lies in the utilization of the so-called capillary-guiding effect [14–25] using tapered capillaries with submicrometer exit diameters [7,23,26–28].

First experiments on guiding of HCIs through straight insulator nanocapillaries showed a remarkable effect: After an initial charge-up phase, the ion beam could be steered by tilting the capillary axis while remaining in the initial charge state. The latter indicates that the transmitted ions never touch the inner walls. Subsequent experiments confirmed this guiding effect also for macroscopic glass capillaries, both straight and tapered ones, suggesting tapered glass capillaries as funnels for HCI beams with unprecedented guiding and focusing properties.

Microscopic simulations for nanocapillaries [29–32] revealed that a self-organized charge up of the capillary walls due to preceding HCI impacts leads to an electric guiding field which steers the incoming projectile ions along the capillary axes. Ion guiding ensues as soon as a dynamical equilibrium of charge up by the ion beam and charge relaxation by bulk or surface conductivity is established. These simulations showed that a stable transmission regime requires a delicate balance between incident ion flux and charge relaxation via surface and bulk conduction. While the processes leading to ion guiding are meanwhile conceptually well understood, applications of this technique as a tool for ion-beam formation and the search for tuning parameters to control and optimize HCI transmission are still in their infancy.

In this paper we show that a key control parameter for guiding is the small residual electric conductivity of the highly insulating capillary material whose dependence of temperature $\sigma(T)$ is nearly exponential [33]. Therefore, guiding can be tuned by only moderate temperature variations near room temperature as first proposed in [34]. We demonstrate that increasing the temperature of a glass capillary and, therefore, its conductivity leads to a reduction of guiding and, eventually, to a complete disappearance of the guiding effect. The strong temperature dependence can be employed to stabilize guiding against Coulomb blockade at high incident ion flux [23,35]. By contrast, at low temperatures, the charge patches deposited on the inner wall of the capillary by the incident beam "freeze out" defocusing the beam and, eventually, blocking transmission.

The plan of the paper is as follows: In Sec. II we report on our measurements of the bulk and surface conductivity of borosilicate glass (Duran), the key parameter for guiding. The experimental setup for macrocapillary guiding is described in Sec. III. Experimental results on its temperature and current dependencies are given in Sec. IV followed by a simplified model description in Sec. V which can semi-quantitatively account for the observed parameter dependencies. A summary and outlook is given in Sec. VI.

*aumayr@iap.tuwien.ac.at

II. CONDUCTIVITY MEASUREMENTS FOR GLASS

We measure the temperature dependence of the electrical conductivity of the capillary material, a borosilicate glass under the trademark Duran [36], following the standard protocol DIN IEC 93 [37]. Both bulk conductivity $\sigma_b(T)$ and surface conductivity $\sigma_s(T)$ are monitored (Fig. 1). The circuit consists of graphite electrodes of circular shape: on the top of the sample a single electrode and at the bottom a smaller circular electrode with the same outer diameter as the top electrode.

The bulk conductivity is measured by grounding the outer ring and applying a voltage U between the other electrodes. The current I is measured with a picoammeter (Keithley 6485). We applied voltages between a few volts and 1 kV with an external power supply (Hewlett Packard 6516A). For determining the surface conductivity, the voltage is applied between the ring and the inner circular electrode. Alternatively, a second geometry was used, where the electrodes were applied to the inside and the outside of a glass tube, respectively. There again, three electrodes were used to determine the bulk and surface conductivities independently. From the applied voltage U and the measured current I, we obtain the specific bulk conductivity

$$\sigma_b = \frac{s}{A}\frac{I}{U}, \tag{1}$$

where s denotes the sample thickness and A the effective area, corresponding to the overlap between the two opposing electrodes. The specific surface conductivity follows as

$$\sigma_s = \frac{g}{L}\frac{I}{U}, \tag{2}$$

where the gap distance between the outer ring and the inner circular electrode is denoted g and L is the effective circumference corresponding to that of the outer ring electrode's inner diameter. In order to avoid any influence from the surroundings the measurements were performed in vacuum. Stainless steel wires held the specimen inside a standard DN 40 CF T-piece which was evacuated prior to the measurements using a turbomolecular pump. The vacuum vessel was heated and cooled from the outside by electrical heaters and a liquid nitrogen bath covering a temperature range from about 255 to 363 K. The actual sample temperature was monitored by a K-type thermocouple which was attached to the glass sample.

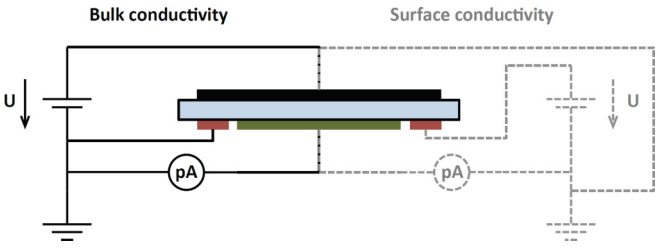

FIG. 1. (Color online) Schematic illustration of the electrical circuit for measuring the bulk conductivity (solid lines) as well as surface conductivity (dashed lines). The glass sample (blue, center) is covered on one side with a circular electrode (black, top). On the bottom side, a ring electrode (red, right and left) is surrounding a central circular electrode (green, center).

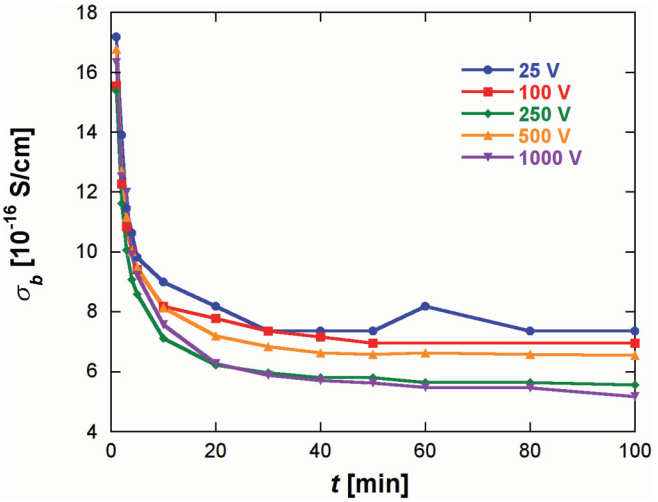

FIG. 2. (Color online) Time dependence of the measured bulk electrical conductivity $\sigma_b(t)$ (different symbols correspond to different applied voltages). The time $t = 0$ corresponds to the time the voltage is turned on.

When applying a voltage to the sample, the time-dependent current approaches a stationary value in an approximately exponential fashion, giving rise to a time-dependent effective conductivity (Fig. 2)

$$\sigma_b(t) = \sigma_{\rm eq} + \Delta\sigma_0 \exp(-At), \tag{3}$$

where the exponential decay rate A and the initial enhancement $\Delta\sigma_0$ are only weakly dependent on the applied voltage. Obviously, charge transport in borosilicate glass is a complex process, mainly mediated by the cationic constituents. The observed time dependence can be attributed to polarization effects (see, e.g., [38] for a topical review).

We find the equilibrium values $\sigma_{\rm eq}$ are somewhat voltage dependent yielding larger σ values for smaller applied voltages. We note parenthetically that this trend is opposed to that predicted for the Poole-Frenkel process [39] indicating that we are well within the linear regime. For the measurement for the temperature dependence $\sigma_{\rm eq}(T)$, we employ in the following a voltage of 100 V. This voltage has been chosen to avoid high field effects on the one hand and electronic noise problems in the very low current regime on the other.

The resulting conductivity for both bulk and surface transport (Fig. 3) displays a steep, approximately exponential, increase with temperature. For comparison, we also show the conductivity data for another borosilicate glass (Pyrex, type 7740) [33]. While for Pyrex $\sigma_b(T)$ is somewhat smaller than for Duran, the temperature dependence, i.e., the slopes, are very close. The near-exponential temperature dependence is key to control guiding by only modest variations of the capillary temperature.

III. EXPERIMENTAL SETUP FOR THE CAPILLARY MEASUREMENTS

Our experimental setup is schematically depicted in Fig. 4 and has been described in detail elsewhere [40]. We use a single straight macroscopic glass capillary (inner diameter 160 μm, outer diameter 300 μm, wall thickness 70 μm,

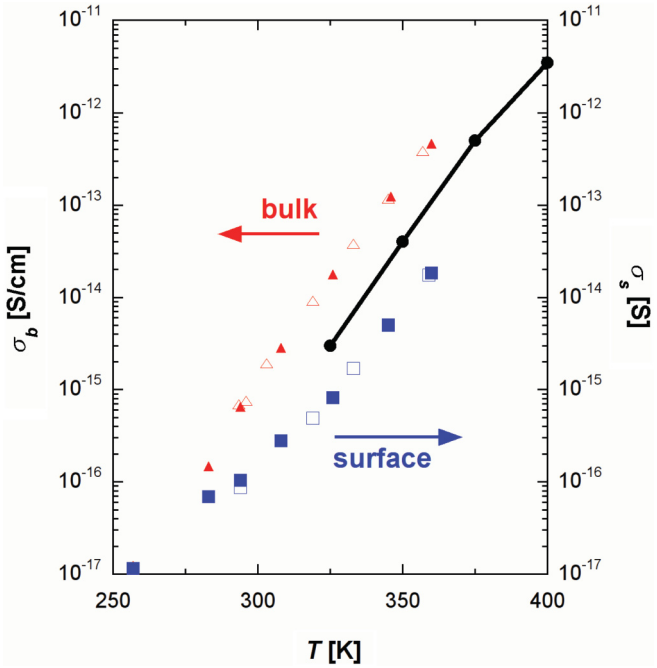

FIG. 3. (Color online) Temperature (T) dependence of the specific electrical conductivity of Duran glass. Triangle (square) symbols denote results for bulk (surface) conductivity measurements. Measurements in vacuum (filled symbols) are compared to corresponding measurements under ambient air (open symbols) conditions. For comparison bulk conductivity values for Pyrex (Type 7740 [33], another borosilicate glass) are shown as black circles (solid line).

macroscopic length 11.4 mm) made of borosilicate glass (Duran) for which the guiding effect has previously been demonstrated [22]. The outside of the capillary is covered with graphite in order to ensure contact with the grounded target holder. While the absolute length of this macrocapillary is much larger than typical nanocapillaries, their aspect ratios length/width ∼70 are quite similar. An oven made of massive copper parts surrounds the capillary in order to guarantee a uniform temperature distribution along the entire tube. The temperature of the copper parts is monitored by a K-type thermocouple. Stainless steel coaxial heaters surrounding the oven are used for heating. Temperatures below room temperature are achieved by cooling the sample holder via heat conduction to a massive UHV copper feedthrough connected to a liquid nitrogen bath outside the UHV chamber, while the sample temperature is stabilized by the proportional-integral-derivative (PID) controlled heaters. Using this setup a temperature range from $-30\,^{\circ}$C up to $90\,^{\circ}$C ($243 \leqslant T \leqslant 363$ K) can be probed. Within such a moderate variation $\Delta T/T \approx 0.3$ the conductivity varies by more than four orders of magnitude (cf. Fig. 3). All measurements were performed under UHV conditions at a base pressure below 5×10^{-9} mbar.

Ar^{7+} ions with a kinetic energy of 4.5 keV are provided by the ECR ion source in Vienna [41]. The extracted ion beam is focused, mass-to-charge separated, and collimated to an angular divergence of less than $\pm 0.5^{\circ}$. A small fraction of the beam passes through a metallic entrance aperture with a diameter of 120 μm directly in front of the capillary. The limiting case of geometric transmission (i.e., without guiding) was calculated from the overlap of a Gaussian beam with a divergence defined by the collimation apertures and the geometric opening of an ideal cylindrical capillary. This calculated transmission profile is almost identical to the transmission profile of a heated (nonguiding) capillary (see Fig. 5). The beam-spot diameter at the aperture is about 2.5 mm. For beam diagnostic and monitoring purposes, a reference aperture (100 μm diameter) can be inserted into the beam instead of the capillary (see Fig. 4). Transmitted ions hit a 50-mm-diameter position sensitive micro-channel-plate detector (PSD) with wedge-and-strip anode, located about 18 cm behind the sample. Charge-state analysis of the transmitted ions is possible by means of a pair of electrostatic deflector plates located near the exit of the capillary. Transmission rates

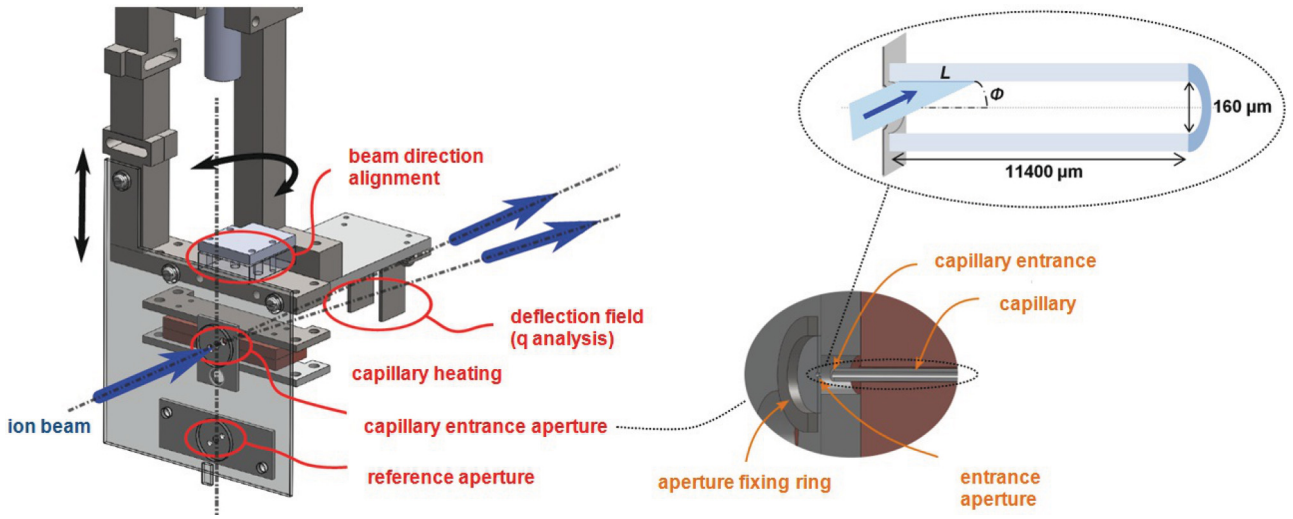

FIG. 4. (Color online) Setup for guiding experiment. The ion beam impinges from the left. It hits the capillary entrance aperture or the reference aperture depending on the z position of the manipulator. Behind the capillary heating unit, containing the sample, the beam is passing a set of vertical deflectors (for charge-state analysis). Approximately 18 cm behind the capillary, a position sensitive micro-channel-plate detector is mounted. Inset: geometry of macrocapillary.

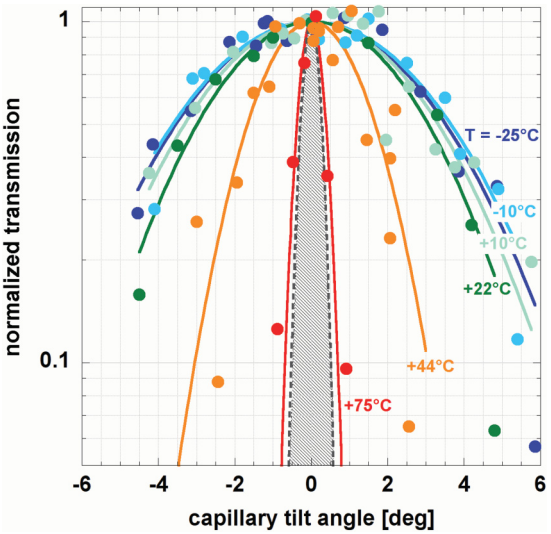

FIG. 5. (Color online) Normalized transmission curves $I(\phi,T)$ for 4.5 keV Ar^{7+} ions guided through a glass capillary for different temperatures ranging from $-25\,^{\circ}$C to $75\,^{\circ}$C (248–348 K). The flux of the incident projectiles was kept constant at about 5000 counts on the PSD in the $\phi = 0^{\circ}$ direction. Gaussian fits through the data points are shown as solid lines. The shaded area indicates the geometric limit of transmission in the absence of guiding.

are recorded after steady-state conditions (i.e., a constant count rate) are reached. The latter does not necessarily imply stable guiding conditions.

IV. EXPERIMENTAL RESULTS

The alignment of the capillary axis relative to the beam corresponding to a tilt angle $\phi = 0^{\circ}$ is determined by maximizing the transmitted intensity I. The tilt angle is then stepwise increased until transmission becomes negligible. Subsequently, the capillary is tilted back stepwise and eventually into the opposite direction (negative ϕ). For each tilt angle the total ion count rate onto the detector is summed up and a dead-time correction is applied. Finally, the transmission as a function of the tilt angle $I(\phi)$ is normalized relative to the transmission at $\phi = 0^{\circ}$ (Fig. 5). The different curves correspond to different capillary temperatures $I(\phi,T)$. The flux of the incident 4.5-keV Ar^{7+} ions was kept constant and corresponds to about 5000 counts on the PSD for the $\phi = 0^{\circ}$ direction. The stability of the ion source was monitored over several hours *before* starting the measurements until intensity fluctuations were negligibly small. The projectile flux entering the capillary was measured before and after each measurement through the reference aperture of the target holder. Additionally, the beam intensity on the collimation diaphragms was constantly monitored during the measurements. Gaussian fits through the data points are shown as solid lines.

The temperature-dependent critical angle $\phi_c(T)$ is determined by the $1/e$ drop of the intensity

$$I(\phi_c,T) = I(0,T)\exp\left[-\phi^2/\phi_c^2(T)\right]. \tag{4}$$

We observe stable optimal guiding conditions near room temperature ($T = 22^{\circ}$ or 295 K) with $\phi_c = 3.5^{\circ}$. Increasing the temperature leads to a considerable narrowing of the transmission function and a corresponding decrease of the critical angle ϕ_c. Eventually, above $75\,^{\circ}$C, $I(\phi,T)$ approaches a temperature-independent transmission function corresponding to the geometric transmission through the capillary ($\pm 0.8^{\circ}$, hatched region in Fig. 5). Due to the elevated conductivity at high temperatures (see Fig. 3) charge patches mediating guiding are quickly removed preventing guiding conditions from being established.

Below room temperature ($T \lesssim 10\,^{\circ}$C) we observe slightly larger $\phi_c(T)$, however, accompanied by dynamical instability of the guided beam (Fig. 6). The transmission angle becomes time dependent and executes random motion. This stochastic motion is a precursor to intermittent blocking. Further cooling to $T = -20\,^{\circ}$C ($\leqslant 250$ K), the time-dependent transmission rapidly fluctuates between maximum and very low transmission (or "blocking"), an effect previously observed for tapered capillaries in [23,27,35]. In addition, the beam spot on the position sensitive detector (resulting from the impact of transmitted ions) moves randomly (Fig. 6). The motion of the center of gravity of the beam spot of transmitted ions is recorded for a capillary tilted by 2° and cooled to $-25\,^{\circ}$C. During the 100-minute-long measurement period (the time

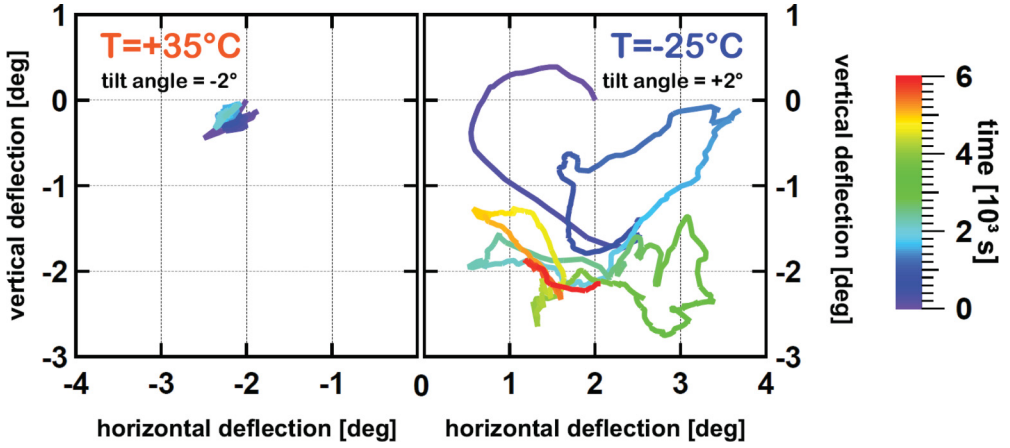

FIG. 6. (Color online) Center-of-gravity motion of an Ar^{7+} beam transmitted through a glass capillary at $T = 35\,^{\circ}$C (left) and $T = -25\,^{\circ}$C (right). In both cases the capillary was tilted by 2°. The elapsed time is indicated by colors: from $t = 0$ (blue) to $t = 6000$ s (red).

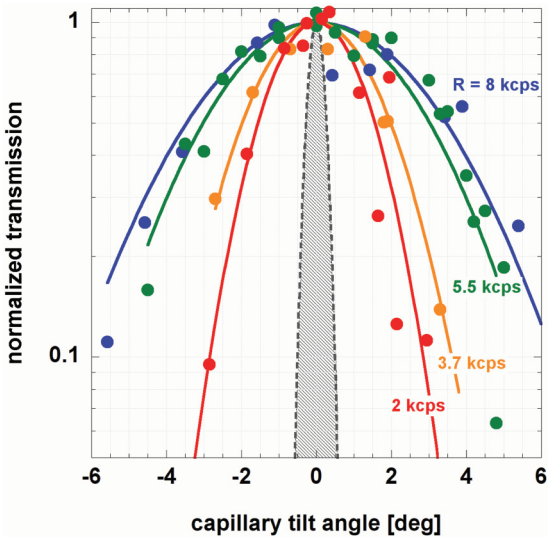

FIG. 7. (Color online) Intensity of the 4.5 keV Ar^{7+} projectile ions transmitted through a single glass capillary at room temperature as a function of capillary tilt angle for different incident current densities j_{in}. Gaussian fits through the data points (normalized to 1 in forward direction) are shown as solid lines. The hatched region indicates the geometric opening of the capillary. The incident current is normalized to the transmitted flux in forward direction ($\phi = 0°$, no guiding) in units of kilocounts per second.

information is color coded) the random motion of the beam spot covers an angular range of almost 4°. This behavior is in strong contrast to that of a hot capillary (35 °C) where the beam spot position is stable over hours showing only small spatial fluctuations associated to the time development of charge patches inside the capillary (left panel in Fig. 6). The wide angular variation of the beam spot at low temperatures suggests strong fluctuations of charge patches. Some of them are most likely located near the capillary exit since the angular range covered exceeds, by far, the geometric opening angle.

A control parameter for the formation of charge patches, complementary to the conductivity, is the incident flux. Keeping the temperature, and thus the conductivity, fixed but varying the incoming current density j_{in} also leads to varying charge patch formation and, hence, varying guiding conditions. Indeed, the transmission curves at fixed T and varying j_{in} (Fig. 7) closely resemble those for varying T (Fig. 5). The critical angle ϕ_c thus becomes a function of both T and j_{in}, $\phi_c(T, j_{in})$.

V. THEORETICAL MODEL

Guiding through nanocapillaries could be successfully simulated in spite of its multiscale nature [29]. These Monte Carlo simulations exploit the fact that the microscopic dynamics is characterized by disparate time scales: Charging by HCIs occurs on the femtosecond scale, the (guided) charge transport on the nanosecond, and the diffusive rearrangement of charges and discharging on a macroscopic time scale (greater than seconds). Extension to macroscopic capillaries where the relevant areas for charge-patch formation are $\sim 10^6$ larger is still a formidable task. Only in the special case of a tapered nontilted capillary ($\phi = 0°$) where azimuthal symmetry is preserved, a microscopic simulation became available [28].

For the present case of a nontapered but tilted macrocapillary, a microscopic simulation of charge-patch formation and guiding is out of reach. Instead, we develop a simplified rate equation model for the first and dominant charge patch assumed to be primarily responsible for establishing stable guiding conditions. A few important differences to nanocapillaries may serve as a guide to specify the relevant parameters entering the rate equation for the glass macrocapillary.

An estimate for the (bulk) diffusion constant for glass based on the Einstein relation

$$\sigma = \frac{1}{\rho} = \frac{ne^2}{kT} D \tag{5}$$

with $n \approx 5.2 \times 10^{19}$ m^{-3} [42] being the number of free charge carriers gives $D_b \approx 3 \times 10^{-16}$ m^2 s^{-1} at room temperature. Charges in glass will therefore diffuse, on average, about 1.3 μm in 10^3 s (1 μm on the surface assuming $D_s = D_b$). This diffusive spread should be compared to the linear extension L of the primary patch along the capillary axis given by the projection of the entrance aperture, $L = 2r/\tan 2° \approx 3500$ μm. Discharging along the surface will therefore be of minor importance and, unlike for nanocapillaries, "bulk" conduction through the thin wall with thickness $d \simeq 70$ μm to the outer surface will dominate. Independent of the underlying transport mechanism (diffusion or field-driven "ohmic" transport) the discharging time τ is inversely related to the conductivity, $\tau^{-1} \propto \sigma_b(T)$, and is thus strongly T dependent (see Fig. 3). Estimates for τ range between about 4 min for ohmic transport to about one month for an unbiased random walk model. Further investigations measuring transport of photoinduced charge carriers through glass plates may help to estimate T more accurately.

We extend and apply now a rate equation model which has been validated by microscopic transport simulations for nanocapillaries [29] to the present case of a macrocapillary. The balance equations for the deposited charge in the primary patch $Q_p(t)$ controlling guiding reads

$$\frac{dQ_p(t)}{dt} = \left(j_{in} - j_{tr} - j_s - \frac{Q_p(t)}{\tau(T)} \right) - \left(\frac{dQ_p(t)}{dt} \right)_{stoc}, \tag{6}$$

where j_{in} is the incoming ion current, j_{tr} is the current transmitted through the capillary, and j_s is the current of scattered projectiles which miss the exit opening of the capillary due to large-angle scattering but hit the opposite side of the capillary eventually forming subsequent patches downstream. We have added the stochastic nonlinear discharge term $(dQ_p/dt)_{stoc}$ in Eq. (6) which will be, in general, a functional of the charging history, $Q_p(t')$ with $t' \leqslant t$, and contributes above a critical value $Q_p(t) > Q_{crit}$. In the regime where a unique stable dynamical equilibrium can be reached this term can be neglected. However, in cases where multivalued hysteresis-like transmission properties appear [43] or no steady state can be reached (see Fig. 6), such corrections become important. Within the regime of stable equilibrium, Eq. (6) is controlled by a single parameter, the discharge time τ.

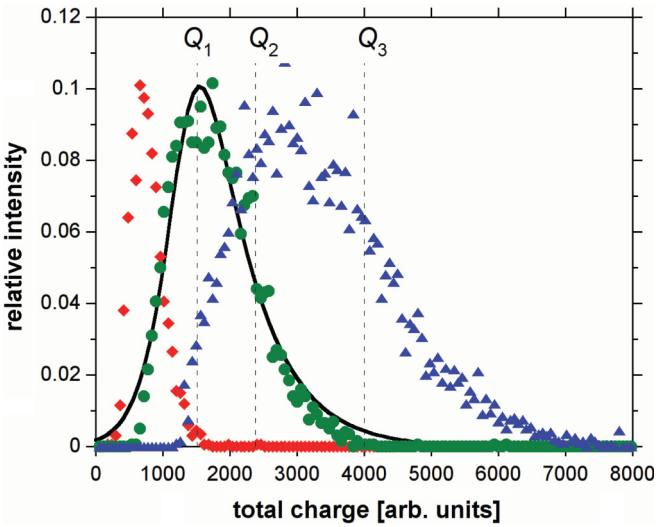

FIG. 8. (Color online) Relative transmission as a function of total charge in the capillary. Incoming projectiles have a kinetic energy of 1.5 keV (red diamonds), 2.5 keV (green circles), and 3.5 keV (blue triangles). The thin solid line is a fit of the data at 2.5 keV to Eq. (9) (cf. text). The incidence angle is $\phi = 2^\circ$, $T = 25\,^\circ$C.

Under equilibrium conditions, i.e., constant transmission along the capillary axis, $j_{\rm tr}$ becomes proportional to $j_{\rm in}$,

$$j_{\rm tr} = f(Q_p,\phi,E,T)j_{\rm in}, \tag{7}$$

where f denotes the fraction of transmitted ions which will, in general, depend on the accumulated charge of the patch Q_p, the tilt angle ϕ, the incident energy E, and the temperature. Consequently, assuming j_s is small at equilibrium (see discussion below) the equilibrium charge is given by

$$Q_p^{(\rm eq)} = j_{\rm in}\tau(T)\left\{1 - f\left(Q_p^{(\rm eq)},\phi,E,T\right)\right\}. \tag{8}$$

Neglecting, for the moment, the dependence of f on Q_p, Eq. (8) predicts that $Q_p^{(\rm eq)}$ controlling guiding is determined by the product of incident current and discharge time, $\alpha(T) = j_{\rm in}\tau(T)$, or, equivalently, by $\alpha(T) \sim j_{\rm in}/\sigma(T)$. Indeed, comparing the experimental temperature dependence (Fig. 5) with the current dependence (Fig. 7) indicates that the dependence of the guiding angle $\phi_c(T, j_{\rm in})$ on T and $j_{\rm in}$ primarily results from its dependence on $\alpha(T)$: Increasing $j_{\rm in}$ and $\sigma(T)$ by the same factor leaves ϕ_c approximately unchanged, in reasonable agreement with Eq. (8). This scaling is independent of the particular functional form of f (to the extent that the Q_p dependence of f can be neglected; see below).

In order to estimate the Q_p dependence of f, we have performed simplified microscopic simulations in which we allow variation of f as a function of Q_p without enforcing the approach to an equilibrium value by decoupling f from $j_{\rm in}$. To this end we allow for continuous charging of the primary patch and its discharging by diffusion into the bulk at a constant rate. For a given Q_p of the patch, we probe f by a Monte Carlo sampling of trajectories where only those contribute to the transmission that directly reach the exit. Large-angle scattered projectiles (j_s) are assumed to have a small probability to be guided to the exit opening and therefore do not contribute to the fraction of transmitted projectiles $j_{\rm tr}$. This approach allows one to probe the transmission function f over a wide range of Q_p far from the equilibrium value $Q_p^{(0)}$, the operating point for stable guiding. In this simulation a capillary with an aspect ratio of 100 was modeled.

Sample results (Fig. 8) for different incident energies indicate that f is a function of the reduced variable $Y = Q_p(t)/E_\perp = Q_p(t)/E\,\sin^2\phi$ as expected for electrostatic deflection and guiding. The observed charge dependence or, for a constant charging rate, time dependence of f suggests a functional form

$$f(Y) = f_0\{\exp[(Y_{\rm on} - Y)/w_{\rm on}] + 1\}^{-1} \times \{\exp[(Y - Y_{\rm off})/w_{\rm off}] + 1\}^{-1}, \tag{9}$$

where $Y_{\rm on}$ is the charging threshold for the onset of deflection and guiding, while $Y_{\rm off}$ is the upper cutoff for guiding and onset of blocking by overcharging. $w_{\rm on,off}$ parametrize the width of the corresponding transitions. Equation (9) fits the simulated data quite well (Fig. 8).

The microscopic process underlying the temporal variation of f (Fig. 8) can be analyzed in terms of the differential

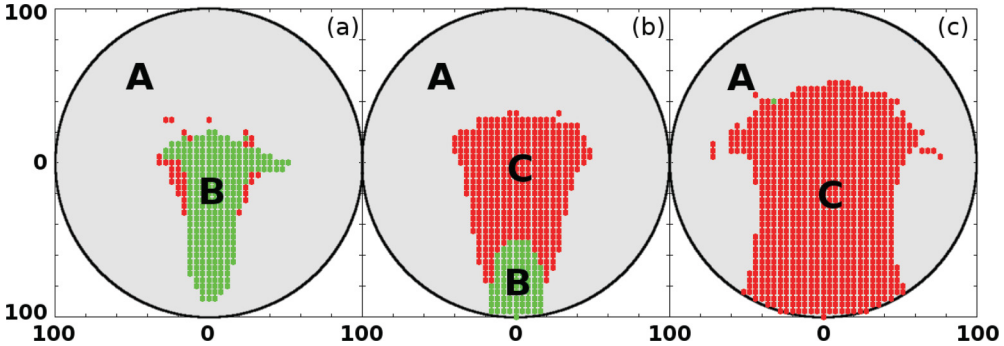

FIG. 9. (Color online) Transmission function f visualized as the fraction of the entrance cross section of the capillary (diameter 200 nm) through which projectiles must enter to be transmitted (area labeled B) for the three charging values Q_i ($i = 1,2,3$) indicated in Fig. 8. Green (grey) dots indicate points within the entrance cross section from where trajectories of projectiles leading to transmission start. Light grey (area A): Projectiles hitting the capillary surface as the Coulomb force of the primary charge patch is not strong enough to deflect them along the capillary axis. Red (dark grey) dots (area C): Projectiles hitting the opposite capillary wall (j_s). (a) Transmission at the maximum of the transmission function (Q_1; cf. Fig. 8), (b) reduced transmission (Q_2, center), and (c) trajectories ending at the capillary wall finally blocking the transmission (charge Q_3, right).

transmission probability resolved over the entrance plane of the capillary (Fig. 9). Monte Carlo simulations for projectiles starting on the entrance plane with a launching angle of $2^\circ \pm 0.5^\circ$ were performed. Depending on the statistics of the termination points of the trajectories the initial conditions are identified as areas A, B, and C. The function f was determined as the fraction of the area of the capillary entrance plane for which the projectile is guided along the capillary axis and transmitted (region B in Fig. 9). Entering the capillary in regions A and C leads to charging the main patch and to the formation of subsequent charge patches, respectively. The peaks in Fig. 8 correspond to the maximum the area B in Fig. 9 can attain. The peak value of f is only weakly dependent on Y (in the present case $f \approx 0.1$) supporting the notion that dynamically stable guiding conditions are, indeed, primarily controlled by $\alpha(T)$ [see Eq. (8)].

In the limit of large α, i.e., either by further reducing the conductivity or increasing the current, a unique dynamical equilibrium can no longer be established (see, e.g., Fig. 6) and Eq. (7) fails. In the case of very large currents j_{in} the limit $Q_p(t) \gg Q_{\text{crit}}$ will be reached and the stochastic discharge term in Eq. (6) will start to contribute leading to sudden discharging events instantaneously reducing the transmission. In the opposite case of reduced conductivity, i.e., at low temperatures, the simple connection between $\alpha(T)$ and the critical angle breaks down as we enter the unstable regime. This onset of dynamical instability can be directly monitored in experiment by the stochastic motion of the beam spot (Fig. 6).

VI. CONCLUSION

We have presented first results on the temperature dependence of macrocapillary transmission which opens the pathway to improved control of ion-beam guiding. Exploiting the strong temperature dependence of the electrical surface and bulk conductivities (almost one order of magnitude per $\Delta T = 25$ K temperature change) allows for optimization of the transmitted beam either for transmitted current or guiding angle of the transmitted beam. Transmission properties of insulating capillaries are governed by the ratio of incident current (charging) and conductivity (discharging) $\alpha(T) = j_{\text{in}}/c\sigma(T)$. By varying the temperature, guiding can be controlled and *reversibly* switched on and off. The improved control over the dynamical equilibrium of charges on the inner capillary wall required for stable transmission conditions due to the strong temperature dependence of $\sigma(T)$ opens up the possibility of improved surface preparation of inner capillary walls. Increasing the conductivity by increasing the temperature promises to overcome one of the obstacles current experimental charged-particle transmission studies face: state-of-the-art cleaning methodology of surface science such as sputtering with keV rare-gas ions cannot be applied due to immediate charge up of the inner surface. Collisional removal of surface deposits (such as hydrocarbons, water, or chemical residues from etching) is suppressed due to deflection at the Coulomb mirror at large distances or Coulomb blocking of the capillary. The present findings suggest that for temperature-resistant materials such as glass, SiO_2, or Al_2O_3 sputtering at elevated temperatures where the dynamical equilibrium for charge up lies below the threshold for guiding for incoming currents j_{in} sufficient for sputtering (small α), cleaning of internal surfaces by sputtering becomes possible. Conventional sputter guns may then be used to clean the surface while keeping the capillary surface uncharged at the same time. This holds the promise for detailed investigations of the influence of the capillary material on ion transmission. Furthermore, our measurements show that monitoring the temperature of capillaries is an important requirement to allow for reproducibility of experimental data sets.

ACKNOWLEDGMENTS

This work has been supported by the European Project ITS-LEIF (No. RII3#026015), by Austrian Science Foundation FWF (SFB041-ViCoM), and in part by the Hungarian Scientific Research Fund OTKA No. NN 103279.

[1] L. P. Ratliff, E. W. Bell, D. C. Parks, A. I. Pikin, and J. D. Gillaspy, Appl. Phys. Lett. **75**, 590 (1999).

[2] E. Akcoltekin, T. Peters, R. Meyer, A. Duvenbeck, M. Klusmann, I. Monnet, H. Lebius, and M. Schleberger, Nat. Nanotechnol. **2**, 290 (2007).

[3] A. S. El-Said, R. Heller, W. Meissl, R. Ritter, S. Facsko, C. Lemell, B. Solleder, I. C. Gebeshuber, G. Betz, M. Toulemonde, W. Möller, J. Burgdörfer, and F. Aumayr, Phys. Rev. Lett. **100**, 237601 (2008).

[4] R. Heller, S. Facsko, R. A. Wilhelm, and W. Möller, Phys. Rev. Lett. **101**, 096102 (2008).

[5] T. Schenkel, A. Persaud, S. J. Park, J. Meijer, J. R. Kingsley, J. W. McDonald, J. P. Holder, J. Bokor, and D. H. Schneider, J. Vac. Sci. Technol. B **20**, 2819 (2002).

[6] J. J. L. Morton, A. M. Tyryshkin, R. M. Brown, S. Shankar, B. W. Lovett, A. Ardavan, T. Schenkel, E. E. Haller, J. W. Ager, and S. A. Lyon, Nature (London) **455**, 1085 (2008).

[7] Y. Iwai, T. Ikeda, T. M. Kojima, Y. Yamazaki, K. Maeshima, N. Imamoto, T. Kobayashi, T. Nebiki, T. Narusawa, and G. P. Pokhil, Appl. Phys. Lett. **92**, 023509 (2008).

[8] F. Aumayr, H. Kurz, D. Schneider, M. A. Briere, J. W. McDonald, C. E. Cunningham, and HP. Winter, Phys. Rev. Lett. **71**, 1943 (1993).

[9] T. Neidhart, F. Pichler, F. Aumayr, HP. Winter, M. Schmid, and P. Varga, Nucl. Instrum. Methods Phys. Res. B **98**, 465 (1995).

[10] M. Tona, H. Watanabe, S. Takahashi, N. Nakamura, N. Yoshiyasu, M. Sakurai, T. Terui, S. Mashiko, C. Yamada, and S. Ohtani, Surf. Sci. **601**, 723 (2007).

[11] M. Tona, Y. Fujita, C. Yamada, and S. Ohtani, Phys. Rev. B **77**, 155427 (2008).

[12] W. Meissl, M. C. Simon, J. R. Crespo Lopez-Urrutia, H. Tawara, J. Ullrich, HP. Winter, and F. Aumayr, Rev. Sci. Instrum. **77**, 093303 (2006).

[13] F. Aumayr, A. S. El-Said, and W. Meissl, Nucl. Instrum. Methods Phys. Res. B **266**, 2729 (2008).

[14] N. Stolterfoht, J.-H. Bremer, V. Hoffmann, R. Hellhammer, D. Fink, A. Petrov, and B. Sulik, Phys. Rev. Lett. **88**, 133201 (2002).

[15] M. B. Sahana, P. Skog, G. Vikor, R. T. Rajendra Kumar, and R. Schuch, Phys. Rev. A **73**, 040901 (2006).

[16] N. Stolterfoht, R. Hellhammer, J. Bundesmann, D. Fink, Y. Kanai, M. Hoshino, T. Kambara, T. Ikeda, and Y. Yamazaki, Phys. Rev. A **76**, 022712 (2007).
[17] R. Hellhammer, J. Bundesmann, D. Fink, and N. Stolterfoht, Nucl. Instrum. Methods Phys. Res. B **258**, 159 (2007).
[18] P. Skog, H. Q. Zhang, and R. Schuch, Phys. Rev. Lett. **101**, 223202 (2008).
[19] N. Stolterfoht, R. Hellhammer, J. Bundesmann, and D. Fink, Phys. Rev. A **77**, 032905 (2008).
[20] N. Stolterfoht, R. Hellhammer, D. Fink, B. Sulik, Z. Juhasz, E. Bodewits, H. M. Dang, and R. Hoekstra, Phys. Rev. A **79**, 022901 (2009).
[21] Y. Kanai, M. Hoshino, T. Kambara, T. Ikeda, R. Hellhammer, N. Stolterfoht, and Y. Yamazaki, Phys. Rev. A **79**, 012711 (2009).
[22] R. J. Bereczky, G. Kowarik, F. Aumayr, and K. Tőkési, Nucl. Instrum. Methods Phys. Res. B **267**, 317 (2009).
[23] R. Nakayama, M. Tona, N. Nakamura, H. Watanabe, N. Yoshiyasu, C. Yamada, A. Yamazaki, S. Ohtani, and M. Sakurai, Nucl. Instrum. Methods Phys. Res. B **267**, 2381 (2009).
[24] N. Stolterfoht, R. Hellhammer, Z. Juhasz, B. Sulik, E. Bodewits, H. M. Dang, and R. Hoekstra, Phys. Rev. A **82**, 052902 (2010).
[25] H. Q. Zhang, P. Skog, and R. Schuch, Phys. Rev. A **82**, 052901 (2010).
[26] T. Ikeda, Y. Kanai, T. M. Kojima, Y. Iwai, T. Kambara, Y. Yamazaki, M. Hoshino, T. Nebiki, and T. Narusawa, Appl. Phys. Lett. **89**, 163502 (2006).
[27] A. Cassimi, T. Muranaka, L. Maunoury, H. Lebius, B. Manil, B. A. Huber, T. Ikeda, Y. Kanai, T. M. Kojima, Y. Iwai, T. Kambara, Y. Yamazaki, T. Nebiki, and T. Narusawa, Int. J. Nanotechnol. **5**, 809 (2008).
[28] T. Schweigler, C. Lemell, and J. Burgdörfer, Nucl. Instrum. Methods Phys. Res. B **269**, 1253 (2011).
[29] K. Schiessl, W. Palfinger, K. Tőkési, H. Nowotny, C. Lemell, and J. Burgdörfer, Phys. Rev. A **72**, 062902 (2005).
[30] K. Schiessl, W. Palfinger, K. Tőkési, H. Nowotny, C. Lemell, and J. Burgdörfer, Nucl. Instrum. Methods Phys. Res. B **258**, 150 (2007).
[31] C. Lemell, K. Schiessl, H. Nowotny, and J. Burgdörfer, Nucl. Instrum. Methods Phys. Res. B **256**, 66 (2007).
[32] K. Schiessl, C. Lemell, K. Tőkési, and J. Burgdörfer, J. Phys.: Conf. Ser. **163**, 12081 (2009).
[33] P. Love, J. Phys. C **16**, 5985 (1983).
[34] N. Bundaleski, H. Khemliche, P. Rousseau, A. Cassimi, L. Maunoury, and P. Roncin, J. Phys.: Conf. Ser. **163**, 012091 (2009).
[35] M. Kreller, G. N. Zschornack, and U. Kentsch, Nucl. Instrum. Methods Phys. Res. B **269**, 1032 (2011).
[36] Duran, available from http://www.duran-group.com
[37] DIN IEC 93, *Prüfverfahren für Elektroisolierstoffe - Spezifischer Durchgangswiderstand und spezifischer Oberflächenwiderstand von festen, elektrisch isolierenden Werkstoffen*, 1983.
[38] A. K. Jonscher, J. Phys. D: Appl. Phys. **32**, R57 (1999).
[39] J. Frenkel, Phys. Rev. **54**, 647 (1938).
[40] R. J. Bereczky, G. Kowarik, K. Tőkési, and F. Aumayr, Nucl. Instrum. Methods Phys. Res. B **279**, 182 (2012).
[41] E. Galutschek, R. Trassl, E. Salzborn, F. Aumayr, and HP. Winter, J. Phys.: Conf. Ser. **58**, 395 (2007).
[42] J. J. Muray, J. Appl. Phys. **33**, 1517 (1962); **33**, 1525 (1962).
[43] T. Ikeda, Y. Kanai, T. M. Kojima, Y. Iwai, Y. Kanazawa, M. Hoshino, T. Kobayashi, G. P. Pokhil, and Y. Yamazaki, J. Phys.: Conf. Ser. **88**, 012031 (2007).